Far-Field Laser Intensity Drop-Outs Caused by Turbulent Boundary Layers

Stanislav Gordeyev, Jacob Cress, and Eric Jumper

Department of Aerospace and Mechanical Engineering,
University of Notre Dame, Notre Dame, Indiana 46556

Usually aero-optical effects are quantified in a time-averaged manner, such as time-averaged spatial root-mean-square of optical path difference or time-averaged Strehl ratio (SR) on a target. However, for airborne free-space, laser-based communication systems, instantaneous SR should be studied as well. An attached transonic boundary layer, for example, provides a relatively high time-average SR; however, experimentally it was discovered that it has many sharp intensity drop-outs, which typically last for a millisecond or so. Left untreated, these drop-outs might lead to significant data loss, potentially slowing down or even disrupting airborne laser-based communications. This paper presents experimentally measured instantaneous near-field wavefront statistics due to laser transmission through subsonic boundary layers. The resulting far-field SR for various flow conditions and aperture sizes are also presented. Using scaling laws for boundary layers, a simple relation between flight conditions and the relative amount of time when the SR drops below a prescribed threshold is developed. The model leads to development of a method for predicting system performance for a free-space communication system. The method is discussed along with possible approaches to using it for designing and optimizing current and future laser-based communication systems. In addition, statistics of the instantaneous drop-outs and analysis of the relative intensity variations caused by boundary layers are presented and discussed.

Nomenclature

Ap	laser beam diameter
$CCDF$	complementary cumulative distribution function
C_f	local skin friction coefficient
C_n^2	index of refraction structure parameter
F_1	function, defined in Eq. (3)
G_A	log-intensity variance aperture function, defined in Eq. (13)
I	intensity on the target
K_{GD}	Gladstone-Dale constant
L	distance to the target

M	Mach number
m	temporal mean of the natural log of $OPD_{rms}(t)$
n'	fluctuating component of refraction index
OPD	optical path difference
OPD_{rms}	spatial root mean square of OPD
OPD_{norm}	normalized OPD, defined in Eq. (6)
OPD_{rms}^{norm}	spatial root mean square of OPD_{norm}
OPL	optical path length
PDF	probability density function
q	dynamic pressure
r_2	ratio between bulk and freestream temperatures
SR	Strehl ratio
s	temporal standard deviation of the natural log of $OPD_{rms}(t)$
t	time
TH	threshold value
TH_{SR}	Strehl ratio threshold value
U_c	convection velocity
x,y,z	coordinate system
Z	$I(t)\,/\,\overline{I(t)}$
γ	viewing angle
δ	boundary-layer thickness
δ^*	boundary-layer displacement thickness
λ	laser wavelength
μ	spatial time-averaged, root mean square of $OPD_{rms}^{norm}(t)$
ρ	freestream density
ρ'	density fluctuations
ρ_{SL}	sea-level density $= 1.225\ \mathrm{kg \cdot m^{-3}}$
$\sigma_{\ln Z}^2$	log-intensity variance
θ	deflection angle or jitter
Σ	standard deviation or spread of $OPD_{rms}^{norm}(t)$
overbar	time averaging

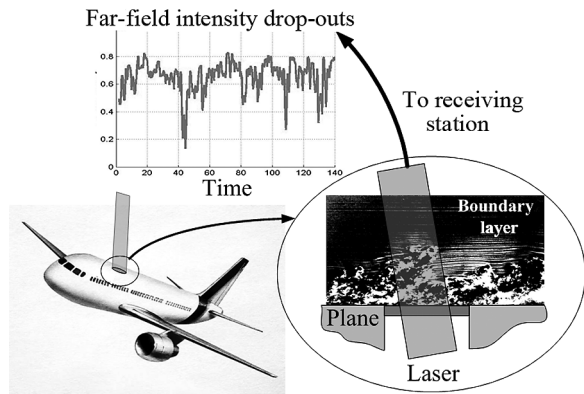## 1. Boundary-Layer Aero-Optical Effects

Laser-based, free-space communication systems have the potential of providing very-high bandwidth, secure lines of communications from air-to-air, air-to-ground and air-to-satellite.[1–3] Because of the system's nominally large field of regard, turrets are used to direct the laser beam toward its target/receiver. Unfortunately, turrets create significant turbulent wakes and therefore variable index of refraction downstream of the turret, which significantly disrupts the outgoing laser beam and, in effect, obscures a significant portion of the field of regard, even at moderate speeds well below transonic.[4] These aero-optical effects[5–7] are typically quantified by the optical path difference, or $OPD(x,y,t)$, over the beam aperture after passing through the turbulent region defined as

$$OPD(x,y,t) = \int_0^\delta n'(x,y,z,t)dz = K_{GD}\int_0^\delta \rho'(x,y,z,t)dz \qquad (1)$$

where n' is the index-of-refraction, ρ' is the density fluctuation field, K_{GD} is the Gladstone-Dale constant, δ is the thickness of the turbulent region, and the z-direction is aligned along the beam propagation direction. The level of aero-optical aberrations are usually described by the spatial root mean square of OPD, or $OPD_{rms}(t)$. The far-field intensity for a large-aperture beam is usually characterized by a Strehl ratio, SR, which is defined as aberrated on-axis light irradiance in the far field divided by the diffraction-limited irradiance. In general, both the diffraction-limited and the distorted beam irradiance in the far field can be calculated using the Fraunhofer approximation.[8]

To avoid large aero-optical effects caused by turrets, system designers have considered placing the pointing-and-tracking turret completely inside of the aircraft, avoiding the problem of separated flow (Fig. 1). Still, the outgoing beam has to pass through a turbulent boundary layer always present on the skin of the aircraft. Density variations inside the compressible boundary layer distort the outgoing beam, resulting in significant intermittent increases in OPD_{rms} and subsequent intensity drop-outs in the far field at the receiver.[9,10] These high-frequency drop-outs, if unchecked, might result in data loss, inevitably slowing or completely disrupting the high-bandwidth data transmission. This is especially true for transonic and supersonic flight speeds.

Fig. 1. Conceptual turret-free, laser-based communication system and boundary-layer–related intensity drop-outs.

Aero-optical properties of turbulent boundary layers have been investigated since the mid-1950s. The first investigation was by Liepmann[11] and made use of the jitter angle of a thin beam of light as it traveled through the compressible, turbulent boundary layers on the sides of high-speed wind tunnels as a way to quantify the crispness of Schlieren photographs. Stine and Winovich[12] performed photometric measurements of the time-averaged radiation field at the focal plane of a receiving telescope. Their work raised the prospect of using optical degradation measurements as a method of inferring turbulence scales. An important analytical tool in studying the aero-optical problem in general was the linking equation, developed by Sutton.[13,14] The equation relates the statistical properties of the turbulent flow to aero-optical distortions. For boundary layers, the average pressure fluctuations are several times smaller than temperature fluctuations[15] so that density fluctuations are at least statistically related to temperature fluctuations only. Under the presumption of negligible pressure fluctuations, these temperature fluctuations, in the case of an adiabatic wall, can be directly calculated from velocity fluctuations using the strong Reynolds analogy (SRA).[16] Rose[17] used the linking equation with these assumptions to estimate aero-optical distortions caused by subsonic turbulent boundary layers by measuring velocity profiles. He found that aero-optical distortions scaled as $OPD_{rms} \sim q\delta$, where q is the dynamic pressure and δ is the

boundary layer thickness. Gilbert[18] performed direct, although time-averaged, aero-optical measurements using an interferometer and compared his results with Rose's data, somewhat validating the linking equation for boundary layers. Masson[19] did a more careful examination of the Gilbert and Rose data and proposed a correction to the linking equation that gave a better comparison; however, his conclusion, similar to Gilbert's, was that the linking equation is essentially valid. Recently, the linking equation was examined using large eddy simulations (LESs) of turbulent boundary layers,[20] and it was concluded that the linking equation is very accurate if the correlation length is defined and evaluated properly. Discrepancies in earlier measurements arise primarily from poor approximations of the correlation length.

Development of accurate high-speed wavefront sensors, such as the Malley probe[21] and high-speed Shack-Hartmann sensors, allow direct and accurate measurements of time and space-resolved aero-optical aberrations. Based on these measurements, it has been firmly established that the structures responsible for aero-optical aberrations in the boundary layer travel at approximately 0.8 to 0.85 of the freestream speed and have streamwise length of the order of several boundary-layer thicknesses.[10,22,23] These and other preliminary conditional measurements[24,25] place the origin of aero-optical structure in the outer region of the boundary layer.

In recent years, several statistics-based models to predict the time-averaged aero-optical distortions of turbulent boundary layers have been developed. Based on extensive aero-optical boundary-layer measurements at various subsonic speeds, M, boundary-layer thicknesses and viewing angles, γ,[10,26] the subsonic boundary-layer aero-optical aberrations for large apertures were found to be

$$OPD_{rms} = 1.7 \cdot 10^{-5} (\rho / \rho_{SL}) M^2 \delta^* / \sin(\gamma) \tag{2}$$

where ρ and ρ_{SL} are the freestream and sea-level densities, respectively; M is the freestream Mach number; and δ^* is the boundary-layer displacement thickness. Based on the measurements in transonic and hypersonic boundary layers, Wyckham and Smits[27] proposed the scaling relation , where C_f is the local skin friction coefficient and r_2 is the ratio between the bulk and freestream temperatures ($r_2 \approx 1$ at subsonic speeds). Gordeyev et al.[22] used the linking equation along with the assumptions of negligible pressure fluctuations and the SRA to predict OPD_{rms} at transonic and supersonic speeds for different Reynolds numbers. They found that

$$OPD_{rms} = 0.2 K_{GD} \rho \delta \sqrt{C_f} F_1(M) \tag{3}$$

where $F_1(M) \approx M^2$ at subsonic speeds. Both models in Gordeyev et al.[22] and Wyckham and Smits[27] were found to generally agree up to $M = 5$ and, at limit of subsonic speeds, they can be reduced to Eq. (2). Extensions for subsonic turbulent boundary layers with nonadiabatic, heated/cooled walls were presented in Cress[10] and Cress et al.[28]

This paper is focused on the temporal statistics of the aero-optical distortions of subsonic turbulent boundary layers, and develops the statistics-based approach to predict the relative amount of the far-field intensity drop-outs. Section 2 describes the experimental setup, and Section 3 describes the data reduction technique and data analysis of $OPD_{rms}(t)$ for various Mach numbers and aperture diameters. The statistical method of calculating a relative percentage of intensity drop-outs for different flight conditions is also presented. Statistics of the drop-out durations and frequency and the analysis of the relative intensity scintillations are also presented and discussed. Conclusions are summarized in the final section.

2. Experimental Setup

The experiments were conducted in the subsonic wind tunnel facility at the U.S. Air Force Academy in Colorado Springs, Colorado. A detailed description of the experimental facilities and experimental procedure can be found in Cress[10] and Cress et al.[26] and only essential details are provided in this paper. The closed-loop tunnel has a test section 2.4 m long with a cross-sectional area of 0.9 m by 0.9 m. The boundary layer on the tunnel walls was approximately 25 mm thick. To measure instantaneous aero-optical distortions caused the subsonic boundary layer, a highly sensitive wavefront sensor called a Malley probe[21] was used. A schematic of the optical setup using the Malley probe is shown at the left in Fig. 2. Two parallel, small-aperture laser beams were traversed through the turbulent flow with boundary layers on the tunnel walls and reflected back along the same path using the return mirror. The returning beams were split off and the jitter signal from each returning beam was measured with a position-sensing device (PSD).

To eliminate the effect of the boundary layer on the opposite wall, an optical insert was used. The narrow optical insert, shown at the right in Fig. 2, was protruded into the boundary-layer flow and effectively allowed the Malley-probe laser beams to bypass the boundary layer on the opposite tunnel wall. The insert was 5 mm thick, protruded 40 mm into the test section, and was 250 mm long in the streamwise direction. The insert was capped with an optically transparent Plexiglas plate 5 mm thick. Laser beams were propagated normal to the test section wall, that is, at 90 degrees relative to the flow direction. The tests were performed for incoming Mach numbers of 0.4 and 0.5. Data were sampled at 100 kHz for 30 seconds.
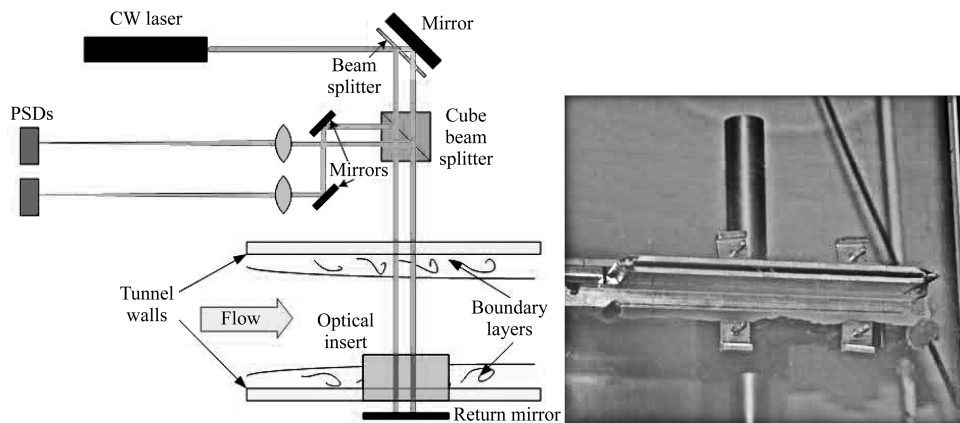

Fig. 2. Schematic of the Malley-probe, single boundary layer setup (left); optical insert (right).

3. Results

3.1. Data reduction

The Malley probe is an optical sensor based on the technique introduced by Malley et al.[29] The operation of this instrument, which is described in detail in Gordeyev et al.,[21] assumes from Huygens' principle that a small-aperture beam which passes through a variable index-

of-refraction field will emerge from that region perpendicular to the wavefront, $W(x,t)$, of a larger beam propagated through the same location at the same moment,

$$\theta(t, x = \text{fixed}) = dW(x,t)/dx = -dOPL(x,t)/dx$$

Here OPL is the optical path length, which is a conjugate or negative of the wavefront and $\theta(t)$ is the time series of the deflection angle of the small-aperture beam. Therefore, a time record of the deflection of the small-aperture beam gives a history of the wavefront slope at that location. If the convection velocity, U_c, of the aberrating structures is known, the OPD can be found using

$$OPL(t) = -U_c \int_{t_0}^{t} (t)dt + Const$$

$$OPD(t) = OPL(t) - \overline{OPL(t)}$$

(4)

where the overbar denotes the time averaging. Using the frozen flow assumption, a one-dimensional streamwise slice of the wavefront as a function of time and the streamwise direction can be found:

$$OPD(t) \rightarrow OPD(t - x/U_c)$$

(5)

The frozen-field approximation assumes no streamwise variation in boundary-layer thickness. While real boundary layers do slowly vary in space, for realistic Reynolds numbers the streamwise variation can be neglected for apertures up to $Ap \sim 10\delta$.[23] Later in this paper we will refer to these large apertures, although not quite correctly, as "infinite" apertures.

Instead of estimating the convection velocity, as done by Malley et al.,[29] the inclusion of the second beam allows the convection velocity to be directly calculated.[21] The jitter signals are correlated in the Fourier domain and the phase relation between the two beams, as a function of frequency, is determined. For a known separation between the two beams, the convection velocity can be found from the slope of the phase/frequency plot.[21]

The reconstruction procedure can be described as follows:

1. The reconstructed wavefront, $OPD(t - x/U_c)$ (Fig. 3(a)), was split into blocks of the same length as the aperture, Ap, by moving the aperture forward in time,

$$OPD(t - x \in [-Ap/2, Ap/2]/U_c) = OPD(x, t; Ap)$$

For simplicity, only adjacent blocks are shown in Fig. 3(b).

2. Spatial piston (mean) and tip-tilt (slopes) were calculated (Fig. 3(b)), and removed from the wavefront for each apertured block (Fig. 3(c)). Thus, only the unsteady component of aero-optical distortions is considered, as they are responsible for intensity variation.

3. The *spatial* root mean square of the optical aberrations, OPD_{rms}, was calculated for each time instant and aperture, resulting in time series of $OPD_{rms}(Ap,t)$ (Fig. 3(d)). By construction, the OPD_{rms} sequence has the same temporal resolution as the original OPD.

4. The time-averaged, spatial root mean square, $\overline{OPD_{rms}(Ap)}$, was calculated for each aperture.
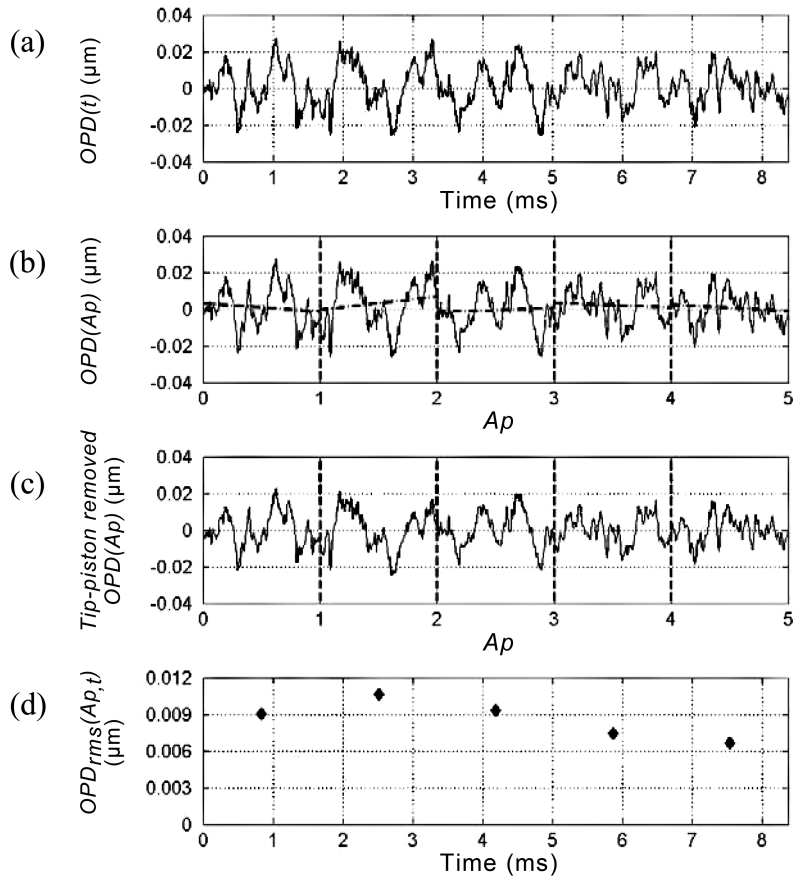
Fig. 3. (a) $OPD(t)$ calculated from deflection angle time trace using Eq. (4); (b) $OPD(t–x/U_c)$ are split in apertured-in-space blocks with the tip-piston across each aperture indicated by the dashed line; (c) tip-piston removed $OPD(x,t;Ap)$, and (d) $OPD_{rms}(t;Ap)$ calculated from the $OPD(x,t;Ap)$ time series.

Although the Malley probe measures only one-dimensional slices of wavefronts, independent two-dimensional wavefront measurements performed on the same boundary layer using a high-speed, Shack-Hartmann sensor[23] and numerical simulations of the turbulent boundary layer[30] confirmed that the Malley probe correctly measures $OPD_{rms}(t)$, the correlation lengths and other wavefront statistical properties. It should be noted that step 2 of the data treatment is critical to the following analysis, as it is equivalent to assuming the presence of a fast steering mirror present in the optical system of sufficient bandwidth to remove the tip/tilt. Siegenthaler[31] has extensively treated the effect of this tip/tilt removal and showed that it is equivalent to a high-pass filter.

Finally, we would like to note that while in the atmospheric optics the aperture is typically normalized by a transverse correlation length; for the boundary layer, the transverse correlation length is not a constant but the function of the aperture itself[10,32] and it is more convenient to normalize the aperture by the boundary-layer thickness.

3.2. Spatial-temporal OPD distribution

Let us define a normalized, aperture-dependent wavefront as

$$OPD_{norm}(x,t; Ap) = \frac{OPD(x,t; Ap)}{OPD_{rms}(Ap = \infty)} \qquad (6)$$

where the wavefront is normalized by the "infinite-aperture," time-averaged value of the OPD_{rms}. Figure 4 shows the probability density function (*PDF*) of $OPD_{norm}(x)$ *in space* for three aperture sizes at M = 0.4 and 0.5. OPD_{norm} is normalized by the spatial time-averaged root mean square of OPD_{norm}, denoted as μ. From Eq. (6) it follows that

$$\mu(Ap) = \frac{\overline{OPD_{rms}(Ap)}}{OPD_{rms}(Ap = \infty)}$$

Thus, it depends on the aperture size only. It is clear from Fig. 4 that within the range of analyzed aperture sizes, $OPD_{norm}(x)$ has a normal distribution regardless of the aperture size. Analysis of two-dimensional wavefronts[23] also confirmed that the spatial wavefront distribution has a normal distribution.
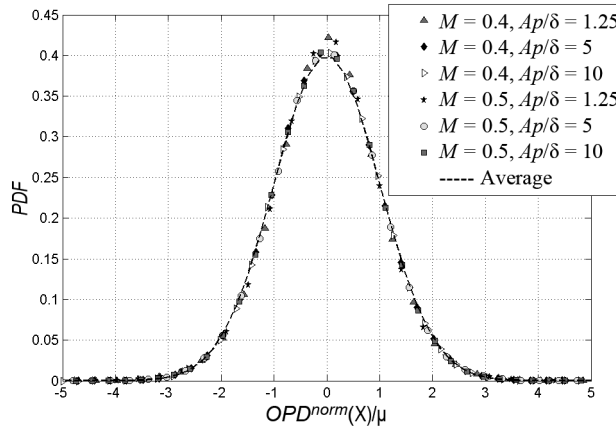

Fig. 4. *PDF* for the $OPD_{norm}(x)$ at M = 0.4 and 0.5 and three aperture sizes plotted as the probability distribution of OPD_{norm}/μ.

If the optical wavefront has a normal distribution in space over the aperture, then the Maréchal formula[33] to calculate the instantaneous Strehl ratio has been shown to be exact for any OPD_{rms}[34]:

$$SR(t) = \exp\left(-\left[\frac{2\pi OPD_{rms}(t)}{\lambda}\right]^2\right) \qquad (7)$$

Thus, for turbulent boundary layers the instantaneous Strehl ratio, $SR(t)$, is directly related to the instantaneous $OPD_{rms}(t)$ via Eq. (7).

3.4. Temporal OPD_{rms} distribution

Figure 5 shows a representative example of $OPD_{rms}(t)$ calculated for the aperture of $Ap = 10\delta$ at the Mach number of 0.5, and the corresponding instantaneous Strehl ratio, $SR(t)$, using the Maréchal formula (Eq. (7)), for two different boundary-layer thicknesses. The time traces show that the instantaneous optical aberrations and the instantaneous Strehl ratio fluctuate significantly about the mean value. Occasionally the fluctuations are noticeably larger, such as the spike at 240 ms at the top in Fig. 5, with the corresponding drop-out in Strehl ratio at the bottom in Fig. 5. These sudden, short-lived spikes are believed to be related to large-scale coherent structures present in the boundary layer,[10] and the corresponding intensity drop-outs were observed to last for several δ/U_∞. The ongoing research investigates a direct link between boundary-layer large-scale structures, which should provide more information about the frequency and the duration of Strehl ratio drop-outs at various boundary-layer parameters and aperture sizes, although preliminary analysis did not reveal any obvious patterns in the frequency of the drop-outs. Thus, these drop-outs might be assumed to be distributed randomly over time.
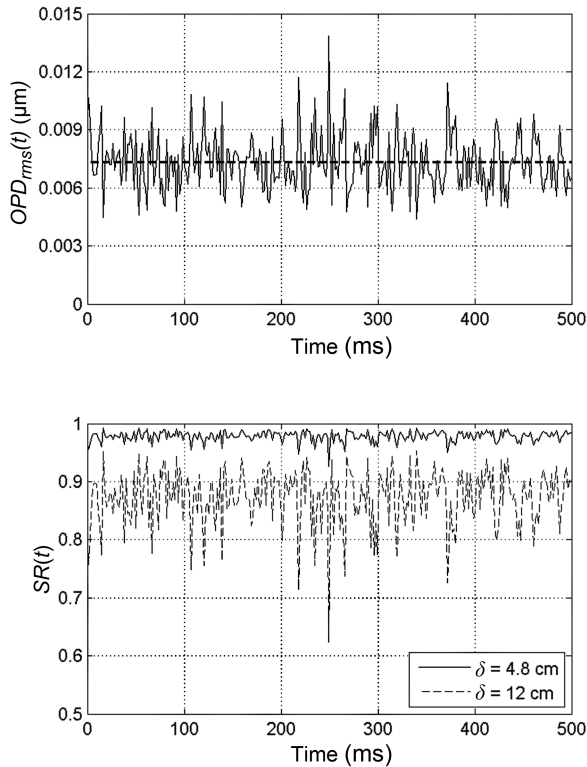

Fig. 5. Time trace of OPD_{rms} over an aperture of $Ap = 10\delta$, $M = 0.5$ (top). Resulting Strehl ratio for a $\delta = 4.8$ cm and 12 cm for the laser wavelength of 1 micron (bottom).

The statistical distribution of $OPD_{rms}(t)$ in time is more relevant than the time traces of $OPD_{rms}(t)$, Fig. 6 at the left shows a *PDF* for the $OPD_{rms}(t)$ for the aperture of $Ap = 10\delta$

for $M = 0.4$ and 0.5. The shape of the *PDF* at each Mach number is well approximated by a log-normal *PDF*:

$$PDF(OPD_{rms}) = \frac{1}{OPD_{rms}\, s\sqrt{2\pi}}\, \exp\left[-\frac{(\ln(OPD_{rms}) - m)^2}{2s^2}\right] \tag{8}$$

where m is the temporal mean and s is the temporal standard deviation of the natural log of $OPD_{rms}(t)$. The dashed lines in Fig. 6 are log-normal distributions where the m and s parameters have been calculated from the experimental data at each Mach number. As these curves show, the log-normal distribution captures the general shape characteristics of the experimental data quite well.

Probability distributions of the normalized, spatial root mean square of $OPD_{norm}(x,t;Ap)$, $OPD_{rms}^{norm}(t)$, for $M = 0.4$ and 0.5 for $Ap = 10\delta$ are shown at the right in Fig. 6. The *PDF*s for various Mach numbers are now collapsed into a single curve, but the shape of the curve is a function of the aperture. Changing the size of the aperture results in different values of the mean and standard deviation for the normalized $OPD_{rms}^{norm}(t)$, which is a direct consequence of the high-pass filter effect of the tip/tilt removal discussed earlier. The values of the temporal mean, μ, and the temporal standard deviation or the spread, Σ, of the $OPD_{rms}^{norm}(t)$ versus the aperture size were calculated from experimental data. These are shown in Fig. 7 for the $M = 0.4$ and 0.5. The slight variation between the different data sets is primarily from experimental errors in the estimation of the boundary-layer thickness. The time-averaged value of $OPD_{rms}(t;Ap)$ monotonically increases with the aperture size and approaches the "infinite" aperture value of $\overline{OPD_{rms}(Ap = \infty)}$; therefore, μ approaches unity when the size of the aperture is increased. From the experimental data it can be observed that this unity value is achieved when the size of the aperture is larger than 8δ. Detailed analysis of aperture effects mentioned earlier can be found in Smith et al.[32] From the plot of the spread, Σ, of the $OPD_{rms}^{norm}(t;Ap)$ in Fig. 7, bottom plot, the spread initially increases as the aperture size increases, but at approximately $Ap = 4\delta$, the value of Σ begins to decrease. The initial increase results from the aperture being smaller than the characteristic size of the optically active structures in the boundary layer. The spread continues to increase as the aperture size increases until several complete optically active structures are within the aperture at a given
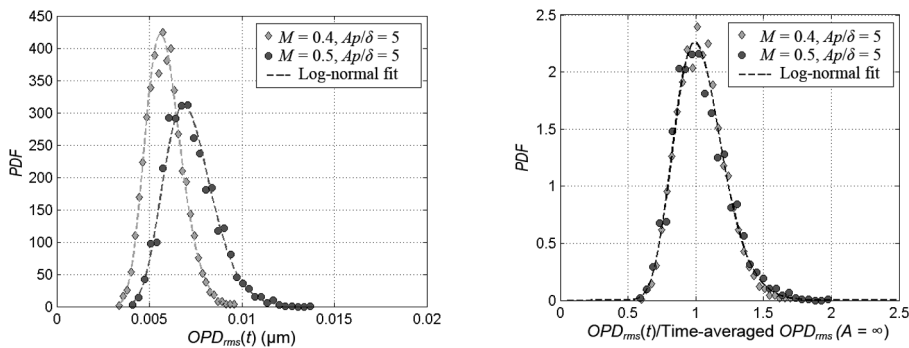

Fig. 6. *PDF* of $OPD_{rms}(t;Ap)$ (left). *PDF* of the normalized $OPD_{rms}(t;Ap)/\overline{OPD_{rms}(Ap = \infty)}$ (right). $M = 0.4$ and 0.5.
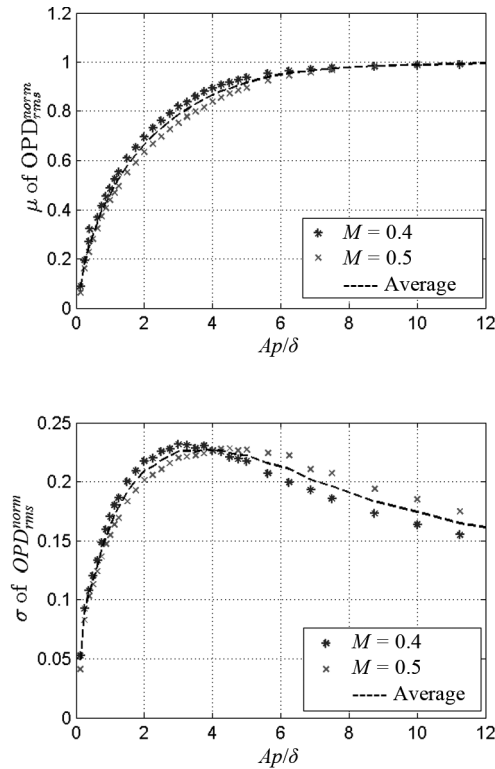
Fig. 7. Temporal mean, μ (top), and spread, Σ, for different aperture sizes at Mach numbers of 0.4 and 0.5 (bottom).

instance (which occurs at approximately 4δ). However, once the aperture is larger than the characteristic size of several optically active structures, the spread of $OPD_{rms}(t;Ap)$ will decrease. It is anticipated that if the aperture were allowed to continue to increase in size until it was infinitely large, the value of the spread, Σ, would go to 0, while the mean value, μ, would become 1; thus, for an infinite aperture, the *PDF* of $OPD_{rms}(t)$ would become the delta function centered at unity. However, as mentioned before, for very large apertures the streamwise variation of the boundary layer should be taken into account and the presented simplified analysis will no longer be valid.

The *PDF* of the $OPD_{rms}^{norm}(t)$, Eq. (8), can be defined in terms of the mean value, μ, and the spread, Σ, which are in turn functions of the aperture size (Fig. 7). These parameters are related to the m and s parameters in Eq. (8) as follows:

$$ m = \log\left(\frac{\mu}{\sqrt{1+(\Sigma/\mu)^2}}\right), \quad s^2 = \log(1+(\Sigma/\mu)^2) \tag{9} $$

Knowing the *PDF* of nondimensional $OPD_{rms}^{norm}(t)$, it is possible to reconstruct the actual *PDF* of *dimensional* $OPD_{rms}(t)$, using Eqs. (8) and (9) for any aperture size, using the data from Fig. 7 and the scaling law for $\overline{OPD_{rms}}(Ap=\infty)$, Eq. (3).

3.5. Instantaneous Strehl ratio

It is often of interest to find the statistical properties of the instantaneous far-field Strehl ratio, such as the percentage of time below a certain threshold value, which is directly related to potential data loss for laser-based communication systems.[1] Note that losing the signal for short periods of time does not necessarily mean losing data, as different encoding schemes, such as interleaving or forward error correction codes can be employed to send a redundant signal and tolerate certain data losses (see Majumdar and Ricklin,[1] for instance). Thus, the signal still can be transmitted through a noisy channel, but it will require decoding to make a redundant signal, inevitably increasing the amount of data to be transmitted to send the original signal. Knowledge of the relative amount of time of intensity drop-outs and drop-out frequencies are helpful in choosing a proper encoding scheme to maximize the *original data* transmission rate.

If a system operates on the absolute value of $SR(t)$, the link is presumed to be lost if the absolute value of $SR(t)$ drops below a prescribed value. Other systems depend on a relative intensity variation, $SR(t)/\overline{SR(t)}$, and the link is considered to be lost if the relative intensity drops below a certain value. In the following, we consider both cases.

Absolute threshold

If optical communication systems require that the laser signal strength at the far-field receiving station remains above a minimum value, the communication link can only reliably operate when the Strehl ratio is above a certain system-defined threshold value, TH_{SR}. Below this threshold value, the link is considered to be broken.

The Maréchal formula, Eq. (7), can be rearranged to solve for OPD_{rms} as a function of SR as

$$OPD_{rms}(t) = \frac{\lambda}{2\pi} \sqrt{-\ln[SR(t)]}$$

or, it can rewritten in terms of the $OPD_{rms}^{norm}(t)$ as

$$OPD_{rms}^{norm}(t) = \frac{\lambda}{2\pi \overline{OPD_{rms}(Ap = \infty)}} \sqrt{-\ln[SR(t)]} \tag{10}$$

Using Eq. (10), the threshold value, TH, can be found as a function of TH_{SR}, the laser wavelength, $OPD_{rms}(Ap = \infty)$ and as follows:

$$TH = \frac{\lambda}{2\pi \overline{OPD_{rms}(Ap = \infty)}} \sqrt{-\ln[TH_{SR}]} \tag{11}$$

If the instantaneous value of the normalized goes *above* the threshold value, TH, then the Strehl ratio goes *below* TH_{SR}, and the optical communication system is considered inoperable and the data are lost. To determine the amount of data lost at the far field, or, equivalently, the total percentage of time that the normalized $OPD_{rms}^{norm}(t)$ is above the given threshold value, TH, the complementary cumulative distribution function (CCDF) can be used. For the log-normal distribution given by Eq. (8), the log-normal CCDF is defined as

$$CCDF(OPD_{rms}^{norm} > TH) = 1 - \frac{1}{2} erfc\left(-\frac{\ln(TH) - m}{s\sqrt{2}}\right) \tag{12}$$

where *erfc* is the complementary error function. Figure 8 shows the CCDF, or the percentage of the $OPD_{rms}^{norm}(t)$ signal above the threshold value, *TH*, for various aperture sizes. For example, for the aperture $Ap = 10\delta$, when the threshold value, *TH*, is <0.5, 100% of the optical aberrations are larger than the threshold value, meaning that in the far field the entire signal will be below the required operational Strehl ratio threshold and no signal will be registered at the receiver. Increasing the threshold value allows durations of the $OPD_{rms}^{norm}(t)$ to begin dropping below the threshold, *TH*, permitting portions of the signal bit stream to reach the far field with an acceptable Strehl ratio. For threshold values, *TH* > 1.8, none of the normalized $OPD_{rms}^{norm}(t)$ is above the threshold, and the entire signal reaches the far field above the threshold Strehl ratio. It is important to note that this limitation on *TH* is stricter than for energy-deposition systems operating only on the time-averaged intensity on the target.

Summarizing, the percentage of data lost due to boundary-layer aero-optical aberrations for given flight conditions and the aperture size can be estimated as follows:

1. Calculate $\overline{OPD_{rms}(Ap = \infty)}$ for the anticipated boundary-layer parameters using Eq. (3). The boundary-layer thickness can be measured experimentally using a hot-wire, Pitot-probe rake, nonintrusive optical measurements,[22] or obtained from numerical or other estimations.

2. For a given threshold of Strehl ratio, $TH_{SR,}$ determine the threshold value, *TH*, for $\overline{OPD_{rms}(Ap = \infty)}$ and the laser wavelength, Σ, using Eq. (11).

3. For the given Ap/δ value, find the mean, μ, and the spread, Σ, values from Fig. 7.

4. Using Eq. (9), calculate the *m* and *s* parameters defining the log-normal distribution of the normalized $OPD_{rms}^{norm}(t)$.

5. Calculate the amount of data lost for the given *m*, *s,* and *TH* parameters using the CCDF(*TH*) function, Eq. (12).

To illustrate the procedure, let us compute the amount data loss for the subsonic boundary layer with the following parameters: boundary layer thickness of $\delta = 10$ cm, $M = 0.8$, altitude of 5000 ft, viewing angle normal to the wall, and $Ap = 5\delta = 0.5$ m. Using Eq. (3), the level of aero-optical distortions would be $\overline{OPD_{rms}(Ap = \infty)} = 0.11$ μm. For a laser wavelength of $\lambda = 1$ μm and the Strehl ratio threshold of $TH_{SR} = 0.5$, from Eq. (11), *TH* can be calculated as 1.2. Finally, Fig. 8 gives the relative amount of time when the intensity is below the threshold as 10%.

If the absolute threshold is given, one can also calculate drop-out durations and time intervals between consecutive drop-outs (a relative occurrence of drop-outs). Probability distributions for drop-out durations and times in between drop-outs for the aperture of Ap/δ = 2.0 for different values of thresholds, *TH*, are presented in Fig. 9. For the large threshold of *TH* = 1.3, the relative amount of the "lost" data is small, about 1%, and the most probable drop-out duration is about $0.5\delta/U_\infty$; the probability distribution for the time interval between drop-outs is wide, indicating the intermittent nature of drop-out events, with average time interval between drop-outs of $20\delta/U_\infty$. When the threshold is decreased to *TH* = 0.9, the amount of "lost" data becomes about 13%. For this threshold, the most probable drop-out duration is still about $0.5\delta/U_\infty$, but the probability tail becomes thicker for this lower threshold, indicating a wider range of drop-out durations. The frequency of drop-out events is increased, with the averaged time interval between drop-outs becoming $4\delta/U_\infty$. When the threshold is decreased even further, to *TH* = 0.6, it results in "losing" almost 60% of the
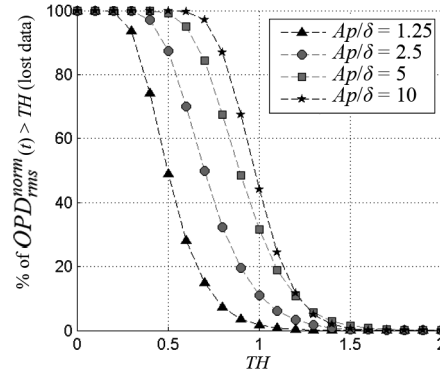
Fig. 8. CCDF of log-normal *PDF* showing the percentage of $OPD_{rms}^{norm}(t)$ that is above the threshold value versus *TH* for various aperture sizes.
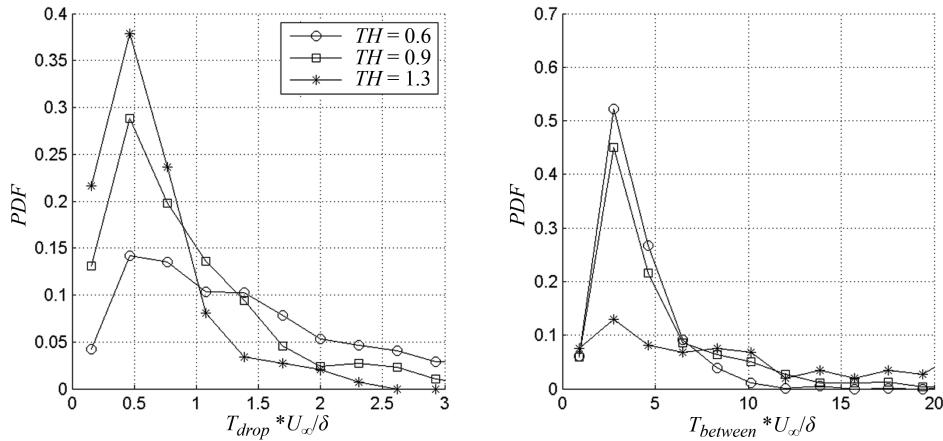

Fig. 9. Probability of the drop-out durations (left), and time interval between successful drop-outs (right) for different threshold values, *TH*.

data, with drop-outs becoming even longer, as the averaged drop-out duration becomes about $2\delta/U_\infty$; the average time between drop-outs is decreased to $3\delta/U_\infty$.

As the typical drop-out duration due to the boundary layer is of the order of the δ/U_∞, or, for a typical transonic boundary layer, of the order of a millisecond, it might potentially result in a loss of several gigabytes of data during the drop-out, thus definitely requiring some sort of interleaving coding scheme to reliably send data through the free-space, laser-based communication channel.

Although the presented analysis is based on the experimental data collected at subsonic speeds of $M = 0.4$ and 0.5, aero-optical properties of the supersonic boundary layers can be extracted from subsonic data, when properly normalized.[22] Therefore, this analysis should, at least approximately, hold for supersonic boundary layers as well.

Relative intensity variation

Optical distortions caused by the beam propagation through atmosphere over long distances result in intensity fluctuations on the target, which are characterized by a relative intensity variation on the target, $Z = I(t)/\overline{I(t)} = SR(t)/\overline{SR(t)}$. For the Kolmogorov-type atmospheric turbulence, these fluctuations have a log-normal distribution and are usually described by the log-intensity variance, $\sigma_{\ln Z}^2 = \overline{(\log Z)^2} - (\overline{\log Z})^2$,[35] and, for weak atmospheric fluctuations and a planar wave, approximately becomes the well-known Rytov variance, $\sigma_{\ln z}^2 \approx 1.23 C_n^2 (2\pi/\lambda)^{7/6} L^{11/6}$.[36] For aero-optical distortions, though, the distribution of the relative intensity variation, Z, is clearly not log-normal, at it follows from Eqs. (7) and (8). Nevertheless, we can still compute the log-intensity variance as a function of the overall level of aero-optical distortions caused by boundary layers, $\overline{OPD_{rms}(Ap = \infty)}$, for different apertures as follows:

$$\sigma_{\ln Z}^2 = \left(2\pi \, \overline{OPD_{rms}(Ap = \infty)}/\lambda\right)^4 \cdot G_A(Ap/\delta) \qquad (13)$$

where $G_A(Ap/\delta) = \exp(4\mu + 4\Sigma^2) \cdot (\exp(4\Sigma^2))$ accounts for finite-aperture effects. The log-intensity variance as a function of the relative aperture size, Ap/δ, and $\overline{OPD_{rms}(Ap = \infty)}/\lambda$, is presented at the left in Fig. 10. The log-intensity variance increases with the increasing OPD_{rms} as the fourth power of OPD_{rms}, or, recalling Eq. (3), as the fourth power of the boundary-layer thickness, δ. Also, it is inversely proportional to the fourth power of the laser wavelength. Clearly, these functional dependencies for boundary-layer, aero-optical–related effects are quite different than for the atmospheric optical effects, expressed in the Rytov variance. In Fig. 10, right, $G_A(Ap/\delta)$ is plotted versus the aperture size. $G_A(Ap/\delta)$ and, therefore, the log-intensity variance initially increases with the aperture size, reach the maximum around $Ap/\delta = 5$ and then start decreasing for larger apertures. Again, this behavior is different from atmospheric optical effects, where the log-normal variance monotonically decreases with aperture size, the so-called aperture-averaging effects (see Tatarski[35] and Andrews et al.,[36] for instance).

Knowing the log-intensity variance caused by turbulent boundary layers, we can compare it to the Rytov variance and find the "equivalent additional" distance the laser beam needs to propagate through the atmosphere to have similar intensity scintillations. Using
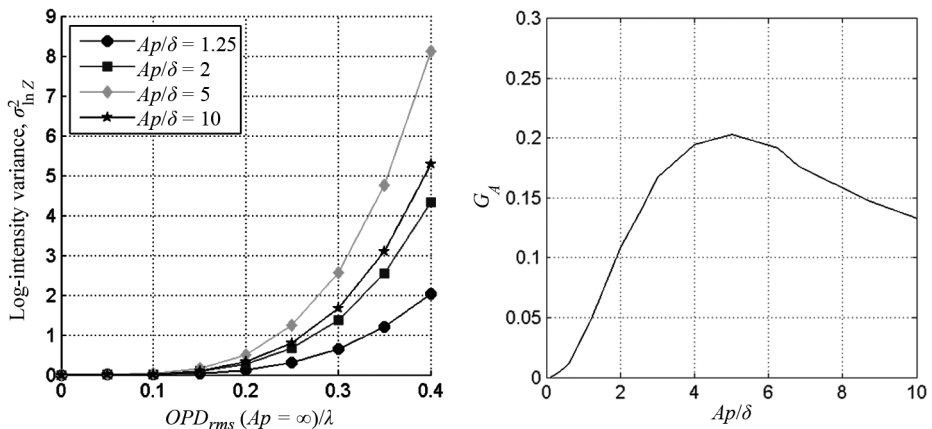

Fig. 10. $\sigma_{\ln Z}^2$ as a function of $\overline{OPD_{rms}(Ap = \infty)}/\lambda$ for different apertures (left). G_A as a function of Ap/δ (right).

boundary-layer parameters from the example in the previous subsection, the log-intensity variance can be calculated using Eq. (13) as = 0.05, and, for a moderately turbulent atmosphere with $C_n^2 = 10^{-14}\,\mathrm{m}^{-2/3}$, the "equivalent additional" distance is approximately 330 m. The same boundary-layer parameters, but at a higher Mach number of $M = 2$, $\sigma_{\ln z}^2$ becomes 7.1, with the "equivalent additional" distance of more than 5 km.

4. Conclusions

The instantaneous aero-optical aberrations caused by subsonic boundary layers were experimentally investigated. The analysis showed that the spatial distribution of $OPD(x)$ over the aperture had a normal distribution. This result confirmed that for optical aberrations caused by the turbulent boundary layer, the on-axis, far-field Strehl ratio can directly calculated using the Maréchal formula. The $OPD_{rms}(t)$ distribution was found to be well-approximated by a log-normal *PDF*. Using the log-normal complementary cumulative distribution function, a procedure was developed to determine the percentage of time when the far-field Strehl ratio is below a prescribed fixed threshold Strehl ratio as a function of given boundary layer parameters and the laser wavelength. In addition, the statistics of durations and the frequency of instantaneous drop-outs for different thresholds were presented and discussed. Finally, results were used to estimate the relative intensity scintillations caused by the boundary layer, and it was shown that the aero-optically-related intensity variations are very different from the ones caused by atmospheric distortions.

This analysis has direct implications for communication applications that depend on the instantaneous intensity of the laser beam in the far field. Performing this analysis on an optical system with given boundary layer conditions would allow a communications engineer to properly size the optical aperture and/or select the appropriate laser wavelength in order to account for additional aero-optical effects caused by boundary layers and achieve an acceptable optical system performance. If the desired performance cannot be achieved due to boundary layer conditions, then this analysis would dictate how the boundary layer must be altered through active or passive control to mitigate the optical aberration effect of the turbulent boundary layer.

Systems that are strictly concerned with delivering high "power in the bucket" at the far field, like direct energy deposition systems, depend on the average value of *SR* and tend to not be affected by the instantaneous fluctuations in the beam intensity. Communication and data link applications, however, are very sensitive to signal dropouts. A broken data link due to the $SR(t)$ dropping below the threshold value requires that either upon reestablishing the connection, the lost data be determined or retransmitted, or the data are sent in a redundant manner using a coding scheme, which also results in the slower data transfer rate. This demonstrates the importance of a consistent, high-quality beam in the far field for communication and data link applications.

As shown, the zero-data-loss requirement poses a stricter limitation on the level of optical aberrations caused by the turbulent boundary layer than an optical communication system can tolerate, as it requires not only the mean value of OPD_{rms} but also the maximum value of $OPD_{rms}(t)$, for a given aperture, to be below a certain threshold. The analysis is based on the frozen flow assumption, and ignores the spatial development of the boundary layer. While this is a safe assumption for smaller apertures, it might lead to incorrect predictions for very large apertures when the boundary layer thickness changes significantly across the aperture. The analysis also neglects any spanwise variation in the optical

aberration, but as shown in Smith et al.,[23] Wang and Wang,[30] and Smith et al.,[32] two-dimensional wavefront aberrations were also correctly predicted by Eq. (2) and the aperture correction. Therefore, any spanwise aperture effects should not greatly affect the statistical results presented.

Due to high spatial and temporal content of the boundary-layer aero-optical aberrations at transonic or supersonic speeds, adaptive optics correction is beyond the capabilities of most current adaptive-optic systems. Thus, beyond the stated limits, one of the practical ways to mitigate boundary-layer aero-optical effects is to continue studying the fundamental physical mechanism behind boundary-layer aero-optical distortions, especially the origin of large intensity drop-outs. Once the specific structures in the boundary layer are quantified, it may be possible to modify their presence and/or character so that aero-optical effects can be mitigated with flow-control strategies, like wall cooling[10] or using passive flow control.[37]

Acknowledgments

References

[1] Majumdar, A.K., and Ricklin, J.C., eds., *Free-Space Laser Communications: Principles and Advances*, Springer (2008).

[2] Scharlemann, E.T., Breitfeller, E.F., Henderson, J.R., et al., Proc. SPIE **5160**, 271 (2004).

[3] Stotts, L.B., Stadler, B., Hughes, D., et al., Proc. SPIE **7464**, 746403 (2009).

[4] Gordeyev, S., and Jumper, E.J., Prog. Aerospace Sci. **46**, 388 (2010).

[5] Gilbert, K.G., Otten, L.J., eds., *Aero-Optical Phenomena*, American Institute of Aeronautics and Astronautics (1982).

[6] Jumper E.J., and Fitzgerald, E.J., Prog. Aerospace Sci. **37**, 299 (2001).

[7] Wang, M., Mani, A., and Gordeyev, S., Annu. Rev. Fluid Mech. **44**, 299 (2012).

[8] Goodman, J.W., *Introduction to Fourier Optics*, 3rd ed., Roberts and Company (2005).

[9] Gordeyev, S., Jumper, E., Ng, T., Cain, A., Aero-Optical Characteristics of Compressible, Subsonic Turbulent Boundary Layer, AIAA Conference Paper 2003-3606 (2003).

[10] Cress, J.A., Optical Aberrations Caused by Coherent Structures in a Subsonic, Compressible, Turbulent Boundary Layer, Ph.D. thesis, University of Notre Dame (2010).

[11] Liepmann, H.W., Deflection and Diffusion of a Light Ray Passing through a Boundary Layer, Tech. Rep. SM-14397, Douglas Aircraft Company, Santa Monica Division, Santa Monica, CA (1952).

[12] Stine, H.A., and Winovich, W., Light Diffusion through High-Speed Turbulent Boundary Layers. Research Memorandum A56B21, National Advisory Committee for Aeronautics, Washington, D.C. (1956).

[13] Sutton G.W., Effects of turbulent fluctuations in an optically active fluid medium, AIAA J. **7**, 1737 (1969).

[14] Sutton G.W., Aero-optical foundations and applications, AIAA J. **23**, 1525 (1985).

[15] Smits, A.J., and Dussauge, J.P., Turbulent shear layers in supersonic flow, American Institute of Physics (1996).

[16] Morkoivin, M.V., Effects of compressibility on turbulent flows, in *Mécanique de la turbulence*, edited by Favre, A., 367 (1962).

[17] Rose, W.C., Measurements of Aerodynamic Parameters Affecting Optical Performance, Air Force Weapons Laboratory Final Report, AFWL-TR-78-191, Kirtland AFB, NM (1979).

[18] Gilbert, K.G., KC-135 aero-optical boundary-layer/shear-layer experiments, in *Aero-Optical Phenomena*, eds., Gilbert, K.G., and Otten, L.J., 306, American Institute of Aeronautics and Astronautics (1982).

[19] Masson, B., Wissler, J., and McMackin, L., Aero-Optical Study of a NC-135 Fuselage Boundary Layer, AIAA Conference Paper 94-0277, January (1994).

[20] Wang, K., and Wang, M., J. Fluid Mech. **696**, 122 (2012).

[21] Gordeyev, S., Hayden, T., and Jumper, E., AIAA J. **45**, 347 (2007).

[22] Gordeyev, S., Jumper, E., and Hayden, T., AIAA J. **50**, 682 (2012).

[23] Smith, A., Gordeyev, S. and Jumper E.J., Recent measurements of aero-optical effects caused by subsonic boundary layers**,** Opt. Eng. **52** (7), 071404, (2013).

[24] Buckner, A., Gordeyev, S., and Jumper, E., Conditional Measurements of Optically-Aberrating Structures in Transonic Attached Boundary Layers, AIAA Conference Paper 2006-0079 (2006).

[25] Wittich, D., Gordeyev, S., and Jumper, E., Revised Scaling of Optical Distortions Caused by Compressible, Subsonic Turbulent Boundary Layers, AIAA Conference Paper 2007-4009 (2007).

[26] Cress, J., Gordeyev, S., and Jumper, E., Aero-Optical Measurements in a Turbulent, Subsonic Boundary Layer at Different Elevation Angles, AIAA Conference Paper 2008-4214 (2008).

[27] Wyckham, C.M., and Smits, A.J., AIAA J. **47**, 2158 (2009).

[28] Cress, J., Gordeyev, S., and Jumper, E., Aero-Optical Measurements in a Heated, Subsonic, Turbulent Boundary Layer, AIAA Paper 2010-0434 (2010).

[29] Malley, M., Sutton, G.W., and Kincheloe, N., Appl. Opt. **31**, 4440 (1992).

[30] Wang, K., and Wang, M., Opt. Eng. **52** (7), 071407 (2013).

[31] Siegenthaler, J.P., Guidelines for Adaptive-Optic Correction Based on Aperture Filtration, Ph.D. thesis, University of Notre Dame (2008).

[32] Smith, A., Gordeyev, S., and Jumper, E., Aperture Effects on Aero-Optical Distortions Caused by Subsonic Boundary Layers, AIAA Conference Paper 2012-2986 (2012).

[33] Mahajan, V., J. Opt. Soc. Am. **73** 860 (1983).

[34] Ross, T.S., Appl. Opt. **48**, 1812 (2009).

[35] Tatarski, V.I., *Wave Propagation in a Turbulent Medium*, McGraw-Hill (1961).

[36] Andrews, L.C., Phillips, R.L., and Hopen, C.Y., *Laser Beam Scintillation with Applications*, SPIE Press (2001).

[37] Smith, A., and Gordeyev S., Evaluation of Passive Boundary Layer Flow Control Methods for Aero-Optic Mitigation, AIAA Conference Paper, 2013-0718 (2013).